

# First search for axion dark matter with a MADMAX prototype

MADMAX Collaboration: B. Ary dos Santos Garcia,<sup>1</sup> D. Bergermann,<sup>1</sup> A. Caldwell,<sup>2</sup> V. Dabhi,<sup>3</sup> C. Diaconu,<sup>3</sup> J. Diehl,<sup>2</sup> G. Dvali,<sup>2</sup> J. Egge,<sup>4</sup> E. Garutti,<sup>4</sup> S. Heyminck,<sup>5</sup> F. Hubaut,<sup>3</sup> A. Ivanov,<sup>2</sup> J. Jochum,<sup>6</sup> S. Knirck,<sup>7</sup> M. Kramer,<sup>5</sup> D. Kreikemeyer-Lorenzo,<sup>2</sup> C. Krieger,<sup>4</sup> C. Lee\*,<sup>2</sup> D. Leppla-Weber,<sup>8</sup> X. Li†,<sup>2</sup> A. Lindner,<sup>8</sup> B. Majorovits,<sup>2</sup> J.P.A. Maldonado,<sup>2</sup> A. Martini,<sup>8</sup> A. Miyazaki,<sup>9</sup> E. Öz,<sup>1</sup> P. Pralavorio,<sup>3</sup> G. Raffelt,<sup>2</sup> J. Redondo,<sup>10</sup> A. Ringwald,<sup>8</sup> J. Schaffran,<sup>8</sup> A. Schmidt,<sup>1</sup> F. Steffen,<sup>2</sup> C. Strandhagen,<sup>6</sup> I. Usherov,<sup>6</sup> H. Wang,<sup>1</sup> and G. Wieching<sup>5</sup>

<sup>1</sup>*III. Physikalisches Institut A, RWTH Aachen University, Aachen, Germany*

<sup>2</sup>*Max-Planck-Institut für Physik, Garching, Germany*

<sup>3</sup>*Aix Marseille Université, CNRS/IN2P3, CPPM, Marseille, France*

<sup>4</sup>*Universität Hamburg, Hamburg, Germany*

<sup>5</sup>*Max-Planck-Institut für Radioastronomie, Bonn, Germany*

<sup>6</sup>*Physikalisches Institut, Eberhard Karls Universität Tübingen, Tübingen, Germany*

<sup>7</sup>*Fermi National Accelerator Laboratory, Batavia, USA*

<sup>8</sup>*Deutsches Elektronen-Synchrotron DESY, Notkestr. 85, 22607 Hamburg, Germany*

<sup>9</sup>*Université Paris-Saclay, CNRS/IN2P3, IJCLab, Orsay, France*

<sup>10</sup>*Universidad de Zaragoza, Zaragoza, Spain*

This paper presents the first search for dark matter axions with mass in the ranges 76.56  $\mu\text{eV}$  to 76.82  $\mu\text{eV}$  and 79.31  $\mu\text{eV}$  to 79.53  $\mu\text{eV}$  using a prototype setup for the MAgnitized Disk and Mirror Axion eXperiment (MADMAX). The experimental setup employs a dielectric haloscope consisting of three sapphire disks and a mirror to resonantly enhance the axion-induced microwave signal within the magnetic dipole field provided by the 1.6 T Morpurgo magnet at CERN. Over 14.5 days of data collection, no axion signal was detected. A 95% CL upper limit on the axion-photon coupling strength down to  $|g_{a\gamma}| \sim 2 \times 10^{-11} \text{GeV}^{-1}$  is set in the targeted mass ranges, surpassing previous constraints, assuming a local axion dark matter density  $\rho_a$  of 0.3  $\text{GeV}/\text{cm}^3$ . This study marks the first axion dark matter search using a dielectric haloscope.

**Introduction**—Axions have become prominent candidates for cold dark matter (DM) [1–4]. They were originally introduced to explain the absence of CP-violating effects in quantum chromodynamics (QCD) through the Peccei-Quinn (PQ) mechanism [5–8]. In the well motivated post-inflationary PQ-symmetry breaking scenario the axion mass required to match the observed DM density is expected to be in the range  $m_a \sim 26$  to 500  $\mu\text{eV}$  for axion models with short-lived domain walls [9–12] or even higher for other models [13, 14]. In the following, the term axion will refer to both, QCD axions and axion-like particles.

In an external magnetic field  $\mathbf{B}_e$ , axions convert to photons and source an oscillating current with frequency corresponding to  $m_a$ , given by  $\mathbf{J}_a = g_{a\gamma} \mathbf{B}_e \dot{a}$  [15] as an additional term to be added to Maxwells’ equations, with  $g_{a\gamma}$  the axion-photon coupling strength and  $\dot{a}$  the temporal derivative of the axion field. Cavity searches are a promising approach to detect axions [16]. They are designed to convert axions from the DM halo into microwave photons using a resonator in a magnetic field. Several cavity searches [17–26] have already put significant constraints on  $|g_{a\gamma}|$  for  $1 \mu\text{eV} \lesssim m_a \lesssim 26 \mu\text{eV}$ , with first efforts being underway to test higher  $m_a$  [27–36], which are challenging to probe with cavity experiments

as their size must be adjusted to match the wavelength of the generated photon. At higher  $m_a$  values, corresponding to higher frequencies of the generated photon, this results in a reduced volume for resonant axion-photon conversion, thereby decreasing sensitivity.

The MAgnitized Disk and Mirror Axion eXperiment (MADMAX) [37–39] makes use of the dielectric haloscope concept to access the well-motivated mass range  $m_a > 26 \mu\text{eV}$ . This concept, based on the magnetized mirror axion DM search idea [40], uses a *booster* composed of a set of parallel dielectric disks and a metallic mirror to enhance a potential axion signal, effectively decoupling the conversion volume from the wavelength and thereby overcoming the limitation of typical cavity experiments towards higher masses.

Due to the large de Broglie wavelength of the considered non-relativistic DM axions of  $\mathcal{O}(10\text{m})$ ,  $\mathbf{J}_a$  is assumed to be uniform over the extent of the booster. This leads to an oscillating electric field uniform across a single medium with dielectric permittivity  $\epsilon$ . The field  $\mathbf{E}_a$  exhibits discontinuities at the boundaries of different media, resulting in the emission of traveling waves with frequency corresponding to  $m_a$  ensuring the continuity of the electric field. The signal power  $P_{\text{sig}}$  due to the coherent emission from multiple surfaces in relation to the power emitted by an ideal magnetized mirror,  $P_0$ , is enhanced by the frequency-dependent boost factor  $\beta^2 = P_{\text{sig}}/P_0$ . By adjusting the disk positions its center frequency and width can be tuned. This makes it pos-

\*Now at LLNL, Livermore, CA, USA

†Now at TRIUMF, Vancouver, Canada

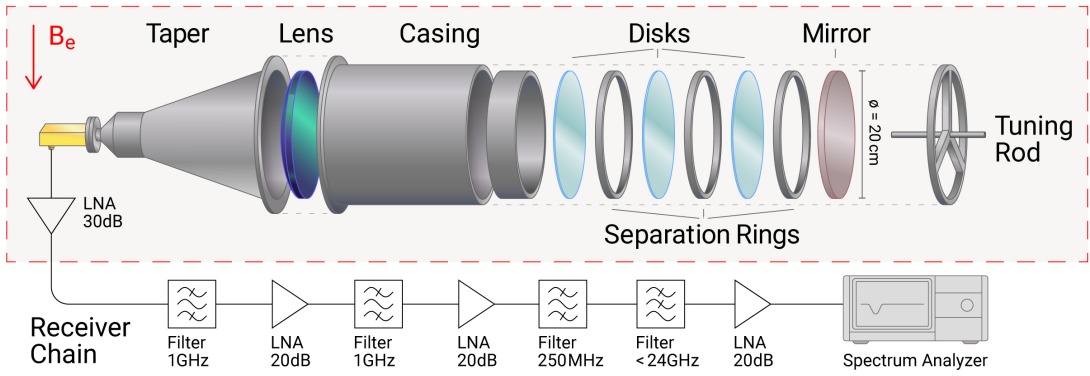


Figure 1: Exploded schematic view of the MADMAX prototype CB200 and the receiver chain. The shaded region represents the components exposed to the B-field.

sible to boost the potential DM axion signal compared to the magnetized mirror concept [40] in dedicated mass ranges. The sensitivity of a MADMAX prototype setup to  $|g_{a\gamma}|$  for a specific signal to noise ratio (SNR) can be estimated as [15]

$$\begin{aligned}
 |g_{a\gamma}| &= 3.5 \times 10^{-11} \text{ GeV}^{-1} \sqrt{\frac{2 \times 10^3}{\beta^2}} \sqrt{\frac{T_{\text{sys}}}{300 \text{ K}}} \\
 &\times \left(\frac{0.1 \text{ m}}{r}\right) \left(\frac{1 \text{ T}}{B_e}\right) \left(\frac{2.2 \text{ days}}{\Delta t}\right)^{1/4} \sqrt{\frac{\text{SNR}}{5}} \quad (1) \\
 &\times \left(\frac{m_a}{80 \text{ } \mu\text{eV}}\right)^{5/4} \sqrt{\frac{0.3 \text{ GeV/cm}^3}{\rho_a}},
 \end{aligned}$$

with system temperature  $T_{\text{sys}}$ , radius  $r$  of the disks and mirror, effective data-taking time  $\Delta t$ , and the local axion DM density  $\rho_a$ .

The MADMAX Collaboration has made significant progress in advancing the development of a future large-scale dielectric haloscope [41–48]. Small-scale setups have successfully validated the dielectric haloscope approach in dark photon DM searches [49, 50], specifically with a broadband MADMAX prototype [50]. This work for the first time demonstrates that a tunable dielectric haloscope can be used to search for axion DM.

**Experimental Setup**— The Closed Booster 200 (CB200) MADMAX prototype is used. As illustrated in Fig. 1, it consists of an aluminum mirror and three sapphire disks of 1 mm thickness, each with a diameter of 200 mm and distanced by separation rings enclosed in an aluminum casing, a Rexolite<sup>®</sup> microwave lens and an aluminum taper, all controlled at  $\mathcal{O}(10 \mu\text{m})$  precision. In contrast to the design used in [50] and envisioned for the final MADMAX design, the prototype is enclosed by conductive boundaries, resulting in fixed boundary conditions, such that only a limited number of cylindrical wave-guide modes within a given frequency range exists inside the booster. This significantly simplifies modeling of the electromagnetic response and allows us to deter-

mine  $\beta^2$  with fewer dedicated measurements. Approximately 84% of the axion induced power couples to the fundamental transverse electric  $\text{TE}_{11}$  mode as calculated by the modal overlap formalism considering the mode of propagation in a wave guide, which is absorbed in the calculation of  $\beta^2$ . The emitted  $\text{TE}_{11}$  power emissions are coupled into the receiver chain by a lens and a specifically designed taper via a  $50 \Omega$  transmission line. The power output of the system is coupled to a heterodyne receiver system, consisting of a series of low noise amplifiers (LNAs) and filters, and a Rohde & Schwarz FSW43 real-time spectrum analyser (SA), which streams time-domain data with  $\sim 0.11 \text{ s}$  coherent integration time to a computer where it is Fourier transformed on GPUs to power spectra. Subsequently, 8047 single power spectra are averaged to individual files with corresponding  $8047 \times 0.11 \text{ s} = 14.75 \text{ min}$  measurement time each. The receiver system has a bandwidth of  $\sim 250 \text{ MHz}$ , which is approximately centred around the respective  $\beta^2$  peak, a resolution of 9 Hz and provides negligible dead-time. It was configured for each run to acquire data around the frequency of the expected maximum  $\beta^2$ . The gain of the receiver chain was calibrated by the Y-factor method [51] using a calibrated noise diode.  $T_{\text{sys}}$  is dominated by the  $\sim 230 \text{ K}$  added noise of the LNA. Additional information on the setup and the methodology used can be found in [52].

Two different disk spacing *configurations* leading to  $\beta^2$  peaks in a  $\sim 10 \text{ MHz}$  range were used to search for axions: Configuration 1 is designed to be sensitive around 18.55 GHz and configuration 2 around 19.21 GHz, corresponding to axion masses around 76.72  $\mu\text{eV}$  and 79.45  $\mu\text{eV}$ , respectively. Frequency adjustment is done by proper choice of the width of separation rings between adjacent disks and between mirror-facing disk and mirror: 12.52 mm, 12.25 mm and 8.38 mm (from left to right in Fig. 1) for configuration 1 and 11.89 mm, 12.25 mm and 8.02 mm for configuration 2. The widths are optimized for a resonance of the  $\text{TE}_{11}$  mode between mirror and

adjacent disk. A  $\mathcal{O}(\mu\text{m})$  change in separation between mirror and closest disk results in  $\mathcal{O}(\text{MHz})$  frequency shift of the  $\beta^2$  distribution. The peak frequencies for both configurations were precisely tuned for different runs to different values by applying mechanical force to the mirror using an adjustable tuning rod. Three *physics-runs* around 18.55 GHz and two around 19.21 GHz were performed, sensitive to different frequency ranges with peak frequencies separated by  $\sim 10$  MHz.

Measurements of CB200 power spectra with a total measurement time of 14.5 days have been performed inside the Morpurgo dipole magnet [53] at CERN. The magnet was operated at field strengths from  $(1.00 \pm 0.01)$  T to  $(1.58 \pm 0.02)$  T.

**Boost factor determination**—The boost factor  $\beta^2$ , which is strongly correlated to the reflectivity  $S_{11}$  of the system [15], and its corresponding uncertainties are determined using a single-mode booster model [52] implemented in ADS [54]. The model is fitted to  $S_{11}$  measurements of the booster. Disk positions, thicknesses, dielectric losses and permittivity are extracted. Losses due to the lens and three-dimensional effects, such as tilts, are modeled by effective dielectric losses.

Identification of the  $\text{TE}_{11}$  booster mode is done for each configuration by measuring the shape of the E-field between mirror and closest disk, using a bead-pull method [45]. It follows the expected shape.  $S_{11}$  measurements confirm the separation of the  $\text{TE}_{11}$  modes from parasitic modes.

The  $\beta^2$  calculation includes the overlap between the theoretical field shape and the uniform axion current of 84%. This is analogous to a form factor in cavity experiments. The uncertainty on the overlap of  $\pm 12\%$  is determined from the deviation between expected and measured field shape obtained from bead-pull measurements.

When measuring power spectra, the experimentally determined  $\sim 41.5 \Omega$  impedance of the first LNA of the receiver chain leads to a mismatch with the transmission line inducing a standing wave between booster and LNA. This modifies  $\beta^2$  obtained from  $S_{11}$  measurements, depending on the distance between the booster and this LNA. The distance is determined from the broadband oscillation pattern induced by resonance of the LNA noise, similar as in [50]. The modeled frequency behavior of the power spectra, adapted to consider the LNA impedance mismatch, matches the measured ones from the physics-runs. Broadband power spectra measurements were taken prior to each physics-run. Drifts in  $T_{\text{sys}}$  or frequency are monitored by comparing the individual 14.75 min long measurements. The variation of the measured booster peak frequencies during physics-runs is used to evaluate the systematic uncertainty on  $\beta^2$ . They follow a Gaussian distribution with a width around 200 kHz for all physics-runs, resulting in an additional uncertainty in  $\beta^2$  for a given frequency of less than 4%.

The extracted boost factors including their uncertainties are shown in Fig. 2. The maximum values for  $\beta^2$  are around 2000, matching expectations [15] and have uncertainties of 13 to 17%.

**Analysis**—The analysis procedure for the MADMAX axion DM search [55] is modeled after the framework established by HAYSTAC [56] and adopts their nomenclature. It combines a set of individual power spectra  $P_i(\nu)$ , each measured with  $\mathcal{O}(14.75 \text{ min})$  averaging time, to a *grand spectrum*, where the full axion signal information is contained in a single bin. The raw FFT data are re-binned for analysis to 0.9 kHz, enough to resolve a potential ALP DM signal.

The spectra  $P_i(\nu)$  are filtered using a fourth-order Savitzky-Golay (SG) filter [57] with a window length of  $\sim 1$  MHz to extract the baselines  $P_{\text{bl},i}(\nu)$ , which are subsequently used to obtain the processed spectra  $p_{\text{proc},i} = (P_i/P_{\text{bl},i} - 1)$ . These processed spectra give local power excesses above the baseline across all frequency bins  $i$ . In the absence of an axion signal and assuming ideal baseline removal, the  $p_{\text{proc},i}$  are expected to follow Gaussian white noise with zero mean and a standard deviation determined by the averaging time. Studies of the full analysis chain applied to simulated data including synthetic axion signals reveal an SNR attenuation due to the SG filter by a factor of  $\eta_{\text{SG}} = 0.95$ , which is constant in the range  $1 < \text{SNR} < 10$ .

The baseline of the recorded power spectra unexpectedly fluctuates on the scale of  $\sim 9$  kHz which introduces unwanted correlations between the processed spectra. This sinusoidal fluctuation is removed by applying a digital notch filter on the inverse Fourier transforms of the  $P_i(\nu)$ . The filter has negligible influence on both amplitude and line-shape of any potential axion signal, while being effective at eliminating the fluctuation artifact. In combination with the SG filter, this process ensures uncorrelated  $p_{\text{proc},i}$ . The  $p_{\text{proc},i}$  are scaled and combined using weights that take the axion sensitivity depending on the B-field strength in individual runs

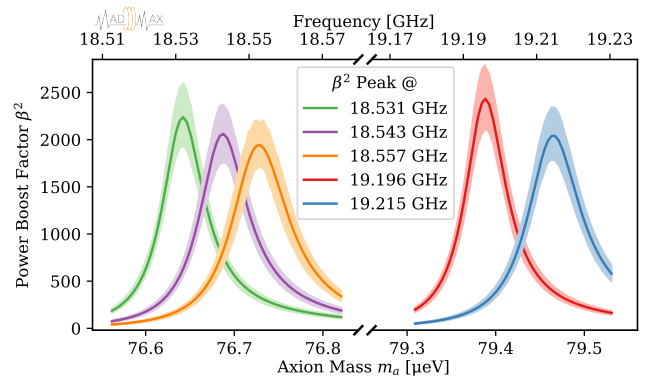


Figure 2: Modeled  $\beta^2$  distributions for the five physics-runs. Lines denote mean  $\beta^2$  and shaded regions give  $\pm 1\sigma$  intervals.

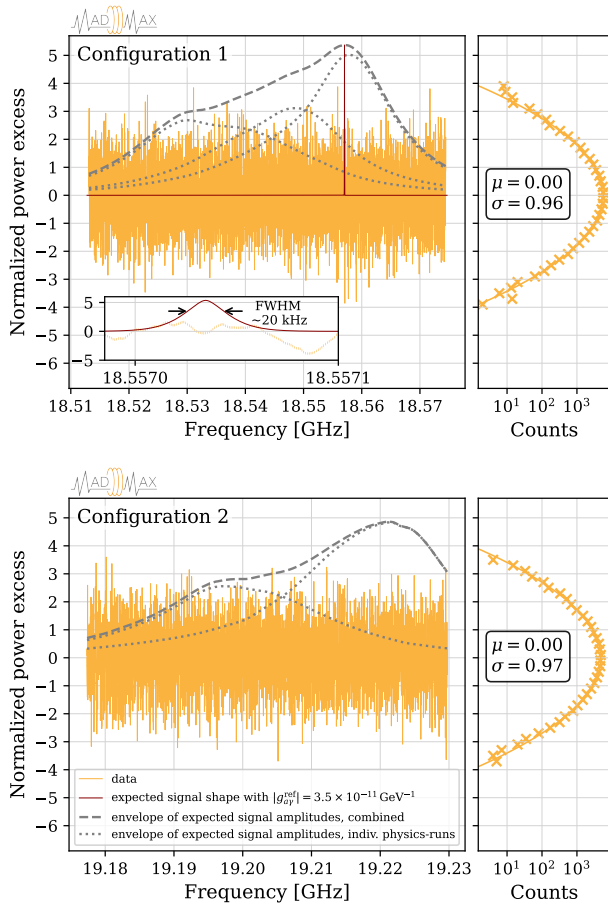


Figure 3: Grand spectra with 0.9kHz bin width for both booster configurations. Dashed gray lines indicate the envelope of expected amplitude in each frequency bin for a reference axion signal with photon coupling of  $|g_{a\gamma}^{\text{ref}}| = 3.5 \times 10^{-11} \text{ GeV}^{-1}$ , combining all physics-runs for both configurations. Dotted lines show the expectation for individual physics runs. The expected signal shape of the same coupling strength at peak sensitivity is shown as solid line. The inset shows a zoom into this mass region. The right panels display histograms of the spectra, overlaid with a best-fit Gaussian distribution with the indicated mean and standard deviation.

into account. The resulting combined spectrum is then cross-correlated with the expected Maxwell-Boltzmann axion line-shape [58, 59] to yield the grand spectrum. A local DM velocity dispersion  $\sigma_v = 156 \text{ km/s}$  [60] and a velocity of the laboratory relative to the DM halo  $v_{\text{lab}} = 242 \text{ km/s}$  [61] are used, resulting in a FWHM of the expected line-shape of  $\sim 20 \text{ kHz}$ .

The grand spectrum is unitless and, in the absence of an axion signal, expected from simulation to have zero mean and a standard deviation of 0.96, slightly below one due to correlations induced by the SG filter [56]. Grand spectra for both configurations are presented in Fig. 3. The gray dashed line shows the envelope of the expected amplitude of excesses, reflecting the SNR of an

Table I: Summary of systematic uncertainties on  $|g_{a\gamma}|$ . Minimum and maximum uncertainties among the frequency range for all physics-runs are reported as first and second values (when necessary). The uncertainty from each physics-run is considered individually when included in the limit estimation.

Effect	Uncertainty in $ g_{a\gamma} $
Y-factor power calibration	3% to 5%
Receiver chain power stability	$\leq 2\%$
Axion field – TE <sub>11</sub> overlap	6%
Boost factor determination (excl. overlap)	$< 5\%$
Frequency stability of TE <sub>11</sub> mode	$< 2\%$
Total	5% to 10%

axion signal with  $|g_{a\gamma}^{\text{ref}}| = 3.5 \times 10^{-11} \text{ GeV}^{-1}$ . Its frequency dependence is determined by a combination of  $T_{\text{sys}}$  and  $\beta^2$ . An axion signal would appear as a narrow localized excess with FWHM of  $\sim 20 \text{ kHz}$ , corresponding to 22 bins at a frequency given by  $m_a$  as shown in the inset. The largest grand spectrum excess observed in both configurations has a local significance of  $4.0\sigma$ , which is consistent with statistical expectations. The probability of an equal or larger excess occurring across the entire dataset assuming no axion signal is  $p = 0.08$ .

Since no evidence of DM axions is found, an upper limit on the axion-photon coupling  $|g_{a\gamma}|$  is derived at 95% Confidence Level (CL) for each 0.9kHz bin as shown in Fig. 4. The individual uncertainty contributions on  $|g_{a\gamma}|$  shown in Table I are propagated into the total uncertainty taking correlations into account. For the  $\beta^2$  determination this is done using Monte Carlo simulation.

The resulting limits on DM axions exceed previous results from the CAST helioscope [62] and astrophysical considerations [63, 64].

**Conclusion**— Searching for axions with a dielectric haloscope, as proposed by the MADMAX collaboration, facilitates accessing the “heavy” axion mass region favored by post-inflationary PQ-symmetry breaking scenarios. A novel boost factor determination method was developed and applied to derive first results from a prototype operated in CERN’s Morpurgo magnet, using the intrinsic advantages offered by the MADMAX approach. Detailed understanding of the radio frequency response of a booster system with closed boundary conditions was demonstrated. The booster could be quickly tuned and re-calibrated to different frequencies demonstrating in principle the opportunity for future larger-range frequency scans. The data from the prototype test campaign using a small booster system inside a modest B-field allow probing for axion dark matter in previously uncharted territory. The achievements presented here and in [50] provide a firm basis for the future research and development program towards a competitive dielectric haloscope, which will include the development of boosters with more and larger dielectric disks, the demonstration

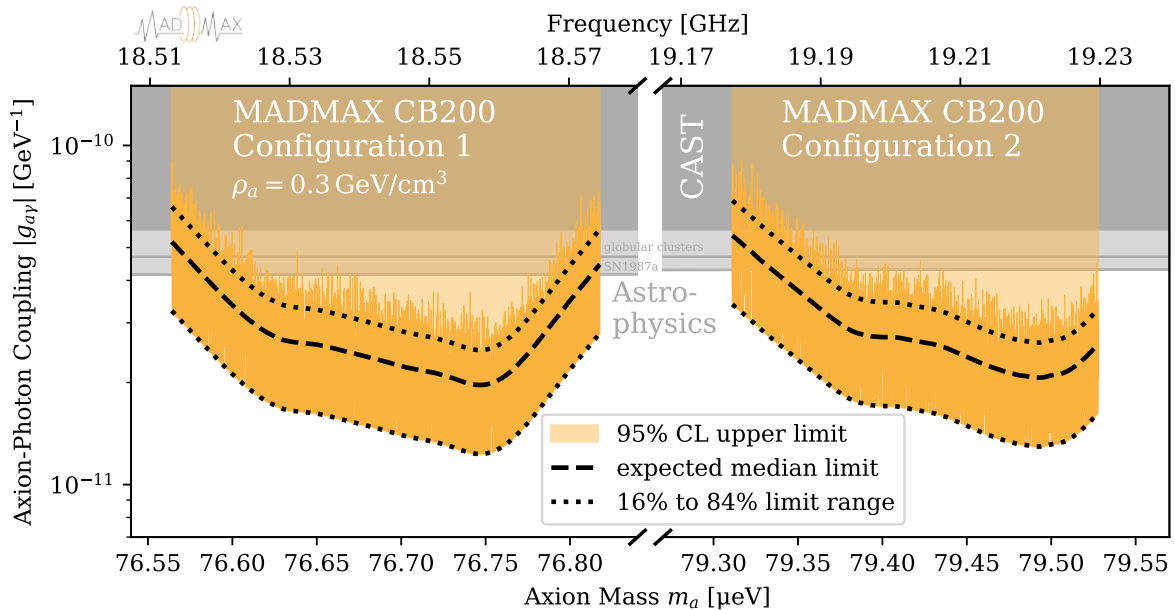


Figure 4: 95% CL exclusion limits in 0.9 kHz bins (orange) from the 2024 MADMAX axion search with the CB200 prototype using the Morpurgo magnet at CERN assuming a local axion DM density of  $\rho_a = 0.3 \text{ GeV cm}^{-3}$ . Limits are compared to the helioscope experiment CAST [62] (dark grey) as well as to supernova [63] and globular cluster limits [64] (light grey). The expected median limit and the 16% and 84% quantiles are shown as black dashed and lower and upper dotted lines, respectively. The limits are truncated below the 16% quantile.

of the calibration and operation of boosters at cryogenic temperatures and the implementation of tuning mechanisms via motorized disk position controls [42, 47, 48]. With ongoing development of a future, unique, large-bore 9 T dipole magnet [46, 65], the MADMAX collaboration is on a very promising track towards probing dark matter QCD axions in the 100  $\mu\text{eV}$  mass region.

**Acknowledgements**—The authors would like to thank the CERN central cryogenic laboratory and the CERN magnet team for the support during all the measurements with the Morpurgo magnet. We are thankful to A. Kazemipour for helping setting up the experiment at CERN and for the RFI measurements performed during data taking. We thank O. Reimann, D. Strom and A. Hambarzumjan for significant contributions during the first phase of the MADMAX project. We thank O. Rossel for providing the drawing of the setup and artistic support. We acknowledge support by the Helmholtz Association (Germany); Deutsche Forschungsgemeinschaft (DFG, German Research Foundation) under Project No. 550641633 and Germany’s Excellence Strategy – EXC 2121 “Quantum Universe” – 390833306. Computations were performed with computing resources granted by RWTH Aachen University under project 7936. SK is supported by Fermi Research Alliance, LLC under Contract No. DE-AC02-07CH11359 with the U.S. Department of Energy, Office of Science, Office of High Energy Physics. We acknowledge the support of the

MADMAX project by the Max Planck Society.

**Data availability**—The data that support the findings of this letter are openly available [66]

- 
- [1] L. F. Abbott and P. Sikivie, *A Cosmological Bound on the Invisible Axion*, *Phys. Lett. B* **120** (1983) 133.
  - [2] M. Dine and W. Fischler, *The Not So Harmless Axion*, *Phys. Lett. B* **120** (1983) 137.
  - [3] J. Preskill, M. B. Wise and F. Wilczek, *Cosmology of the Invisible Axion*, *Phys. Lett. B* **120** (1983) 127.
  - [4] I. G. Irastorza and J. Redondo, *New experimental approaches in the search for axion-like particles*, *Prog. Part. Nucl. Phys.* **102** (2018) 89 [1801.08127].
  - [5] R. D. Peccei and H. R. Quinn, *CP Conservation in the Presence of Pseudoparticles*, *Phys. Rev. Lett.* **38** (1977) 1440.
  - [6] R. D. Peccei and H. R. Quinn, *Constraints imposed by CP conservation in the presence of pseudoparticles*, *Phys. Rev. D* **16** (1977) 1791.
  - [7] S. Weinberg, *A new light boson?*, *Phys. Rev. Lett.* **40** (1978) 223.
  - [8] F. Wilczek, *Problem of Strong P and T Invariance in the Presence of Instantons*, *Phys. Rev. Lett.* **40** (1978) 279.
  - [9] V. B. Klaer and G. D. Moore, *The dark-matter axion mass*, *JCAP* **11** (2017) 049 [1708.07521].
  - [10] M. Gorghetto, E. Hardy and G. Villadoro, *More axions from strings*, *SciPost Phys.* **10** (2021) 050 [2007.04990].
  - [11] M. Buschmann, J. W. Foster, A. Hook, A. Peterson,

- D. E. Willcox, W. Zhang et al., *Dark matter from axion strings with adaptive mesh refinement*, *Nature Commun.* **13** (2022) 1049 [2108.05368].
- [12] K. Saikawa, J. Redondo, A. Vaquero and M. Kaltschmidt, *Spectrum of global string networks and the axion dark matter mass*, *JCAP* **10** (2024) 043 [2401.17253].
- [13] A. Ringwald and K. Saikawa, *Axion dark matter in the post-inflationary Peccei-Quinn symmetry breaking scenario*, *Phys. Rev. D* **93** (2016) 085031 [1512.06436].
- [14] K. A. Beyer and S. Sarkar, *Ruling out light axions: The writing is on the wall*, *SciPost Phys.* **15** (2023) 003 [2211.14635].
- [15] A. J. Millar, G. G. Raffelt, J. Redondo and F. D. Steffen, *Dielectric Haloscopes to Search for Axion Dark Matter: Theoretical Foundations*, *JCAP* **01** (2017) 061 [1612.07057].
- [16] P. Sikivie, *Experimental Tests of the Invisible Axion*, *Phys. Rev. Lett.* **51** (1983) 1415.
- [17] ADMX collaboration, N. Du et al., *A Search for Invisible Axion Dark Matter with the Axion Dark Matter Experiment*, *Phys. Rev. Lett.* **120** (2018) 151301 [1804.05750].
- [18] ADMX collaboration, T. Braine et al., *Extended Search for the Invisible Axion with the Axion Dark Matter Experiment*, *Phys. Rev. Lett.* **124** (2020) 101303 [1910.08638].
- [19] ADMX collaboration, C. Bartram et al., *Search for Invisible Axion Dark Matter in the 3.3–4.2  $\mu\text{eV}$  Mass Range*, *Phys. Rev. Lett.* **127** (2021) 261803 [2110.06096].
- [20] Y. Kim et al., *Experimental Search for Invisible Dark Matter Axions around 22  $\mu\text{eV}$* , *Phys. Rev. Lett.* **133** (2024) 051802 [2312.11003].
- [21] CAPP collaboration, S. Ahn et al., *Extensive Search for Axion Dark Matter over 1 GHz with CAPP'S Main Axion Experiment*, *Phys. Rev. X* **14** (2024) 031023 [2402.12892].
- [22] TASEH collaboration, H. Chang et al., *First Results from the Taiwan Axion Search Experiment with a Haloscope at 19.6  $\mu\text{eV}$* , *Phys. Rev. Lett.* **129** (2022) 111802 [2205.05574].
- [23] B. M. Brubaker et al., *First results from a microwave cavity axion search at 24  $\mu\text{eV}$* , *Phys. Rev. Lett.* **118** (2017) 061302 [1610.02580].
- [24] HAYSTAC collaboration, L. Zhong et al., *Results from phase 1 of the HAYSTAC microwave cavity axion experiment*, *Phys. Rev. D* **97** (2018) 092001 [1803.03690].
- [25] HAYSTAC collaboration, K. M. Backes et al., *A quantum-enhanced search for dark matter axions*, *Nature* **590** (2021) 238 [2008.01853].
- [26] C. M. Adair et al., *Search for Dark Matter Axions with CAST-CAPP*, *Nature Commun.* **13** (2022) 6180 [2211.02902].
- [27] RADES collaboration, A. A. Melcón et al., *First results of the CAST-RADES haloscope search for axions at 34.67  $\mu\text{eV}$* , *JHEP* **21** (2020) 075 [2104.13798].
- [28] A. P. Quiskamp, B. T. McAllister, P. Altin, E. N. Ivanov, M. Goryachev and M. E. Tobar, *Direct search for dark matter axions excluding ALPogenesis in the 63- to 67- $\mu\text{eV}$  range with the ORGAN experiment*, *Sci. Adv.* **8** (2022) abq3765 [2203.12152].
- [29] A. Quiskamp, B. T. McAllister, P. Altin, E. N. Ivanov, M. Goryachev and M. E. Tobar, *Exclusion of Axionlike-Particle Cogenesis Dark Matter in a Mass Window above 100  $\mu\text{eV}$* , *Phys. Rev. Lett.* **132** (2024) 031601 [2310.00904].
- [30] QUAX collaboration, R. Di Vora et al., *Search for galactic axions with a traveling wave parametric amplifier*, *Phys. Rev. D* **108** (2023) 062005 [2304.07505].
- [31] QUAX collaboration, A. Rettaroli et al., *Search for axion dark matter with the QUAX-LNF tunable haloscope*, *Phys. Rev. D* **110** (2024) 022008 [2402.19063].
- [32] F. Bajjali et al., *First results from BRASS-p broadband searches for hidden photon dark matter*, *JCAP* **08** (2023) 077 [2306.05934].
- [33] BREAD collaboration, S. Knirck et al., *First Results from a Broadband Search for Dark Photon Dark Matter in the 44 to 52  $\mu\text{eV}$  Range with a Coaxial Dish Antenna*, *Phys. Rev. Lett.* **132** (2024) 131004 [2310.13891].
- [34] M. Lawson, A. J. Millar, M. Pancaldi, E. Vitagliano and F. Wilczek, *Tunable axion plasma haloscopes*, *Phys. Rev. Lett.* **123** (2019) 141802 [1904.11872].
- [35] B. Aja et al., *The Canfranc Axion Detection Experiment (CADEx): search for axions at 90 GHz with Kinetic Inductance Detectors*, *JCAP* **11** (2022) 044 [2206.02980].
- [36] DALI collaboration, J. De Miguel, J. F. Hernández-Cabrera, E. Hernández-Suárez, E. Joven-Álvarez, C. Otani and J. A. Rubiño Martín, *Discovery prospects with the Dark-photons & Axion-like particles Interferometer*, *Phys. Rev. D* **109** (2024) 062002 [2303.03997].
- [37] J. Jaeckel and J. Redondo, *Resonant to broadband searches for cold dark matter consisting of weakly interacting slim particles*, *Phys. Rev. D* **88** (2013) 115002 [1308.1103].
- [38] A. Caldwell, G. Dvali, B. Majorovits, A. Millar, G. Raffelt, J. Redondo et al., *Dielectric Haloscopes: A New Way to Detect Axion Dark Matter*, *Phys. Rev. Lett.* **118** (2017) 091801 [1611.05865].
- [39] MADMAX collaboration, P. Brun et al., *A new experimental approach to probe QCD axion dark matter in the mass range above 40  $\mu\text{eV}$* , *Eur. Phys. J. C* **79** (2019) 186 [1901.07401].
- [40] D. Horns, J. Jaeckel, A. Lindner, A. Lobanov, J. Redondo and A. Ringwald, *Searching for WISPy Cold Dark Matter with a Dish Antenna*, *JCAP* **04** (2013) 016 [1212.2970].
- [41] S. Knirck, J. Schütte-Engel, A. Millar, J. Redondo, O. Reimann, A. Ringwald et al., *A First Look on 3D Effects in Open Axion Haloscopes*, *JCAP* **08** (2019) 026 [1906.02677].
- [42] J. Egge, S. Knirck, B. Majorovits, C. Moore and O. Reimann, *A first proof of principle booster setup for the MADMAX dielectric haloscope*, *Eur. Phys. J. C* **80** (2020) 392 [2001.04363].
- [43] MADMAX collaboration, S. Knirck et al., *Simulating MADMAX in 3D: requirements for dielectric axion haloscopes*, *JCAP* **10** (2021) 034 [2104.06553].
- [44] J. Egge, *Axion haloscope signal power from reciprocity*, *JCAP* **04** (2023) 064 [2211.11503].
- [45] J. Egge et al., *Experimental determination of axion signal power of dish antennas and dielectric haloscopes using the reciprocity approach*, *JCAP* **04** (2024) 005

- [2311.13359].
- [46] C. Lorin, W. A. Maksoud, J. Allard, C. Berriaud, V. Calvelli, L. Denarie et al., *Development, Integration, and Test of the MACQU Demo Coil Toward MADMAX Quench Analysis*, *IEEE TAS* **33** (2023) 1.
- [47] E. Garutti, H. Janssen, D. Kreikemeyer-Lorenzo, C. Krieger, A. Lindner, B. Majorovits et al., *Qualification of piezo-electric actuators for the MADMAX booster system at cryogenic temperatures and high magnetic fields*, *JINST* **18** (2023) P08011 [2305.12808].
- [48] MADMAX collaboration, B. Ary Dos Santos Garcia et al., *First mechanical realization of a tunable dielectric haloscope for the MADMAX axion search experiment*, *JINST* **19** (2024) T11002 [2407.10716].
- [49] R. Cervantes et al., *ADMX-Orpheus first search for 70  $\mu\text{eV}$  dark photon dark matter: Detailed design, operations, and analysis*, *Phys. Rev. D* **106** (2022) 102002 [2204.09475].
- [50] MADMAX collaboration, J. Egge et al., *First Search for Dark Photon Dark Matter with a MADMAX Prototype*, *Phys. Rev. Lett.* **134** (2025) 151004 [2408.02368].
- [51] D. Pozar, *Microwave Engineering*. Wiley, 2011.
- [52] See supplemental material at [URL] for additional information on the overlap formalism, preparation and verification of the booster mode, the experimental setup used at CERN, data taking, power calibration and booster noise modelling. The supplemental material also contains [67].
- [53] M. Morpurgo, *A large superconducting dipole cooled by forced circulation of two phase helium*, *Cryogenics* **19** (1979) 411.
- [54] Keysight, “ADS advanced design system.” <https://www.keysight.com/de/de/products/software/pathwave-design-software/pathwave-advanced-design-system.html>.
- [55] J. Diehl, *Statistical Methods for a First MADMAX Axion Dark Matter Search and Beyond*, Ph.D. thesis, Technical University Munich, 2024, Available at <https://mediatum.ub.tum.de/?id=1752277>.
- [56] B. M. Brubaker, L. Zhong, S. K. Lamoreaux, K. W. Lehnert and K. A. van Bibber, *HAYSTAC axion search analysis procedure*, *Phys. Rev. D* **96** (2017) 123008 [1706.08388].
- [57] A. Savitzky and M. J. E. Golay, *Smoothing and differentiation of data by simplified least squares procedures*, *Analytical Chemistry* **36** (1964) 1627.
- [58] C. A. J. O’Hare and A. M. Green, *Axion astronomy with microwave cavity experiments*, *Phys. Rev. D* **95** (2017) 063017 [1701.03118].
- [59] J. Diehl, J. Knollmüller and O. Schulz, *Bias-free estimation of signals on top of unknown backgrounds*, *Nucl. Instrum. Meth. A* **1063** (2024) 169259 [2306.17667].
- [60] M. S. Turner, *Periodic signatures for the detection of cosmic axions*, *Phys. Rev. D* **42** (1990) 3572.
- [61] J. Bovy, C. Allende Prieto, T. C. Beers, D. Bizyaev, L. N. da Costa, K. Cunha et al., *The Milky Way’s Circular-velocity Curve between 4 and 14 kpc from APOGEE data*, *Astrophys. J.* **759** (2012) 131 [1209.0759].
- [62] CAST collaboration, K. Altenmüller et al., *New Upper Limit on the Axion-Photon Coupling with an Extended CAST Run with a Xe-Based Micromegas Detector*, *Phys. Rev. Lett.* **133** (2024) 221005 [2406.16840].
- [63] C. A. Manzari, Y. Park, B. R. Safdi and I. Savoray, *Supernova axions convert to gamma rays in magnetic fields of progenitor stars*, *Phys. Rev. Lett.* **133** (2024) 211002.
- [64] M. J. Dolan, F. J. Hiskens and R. R. Volkas, *Advancing globular cluster constraints on the axion-photon coupling*, *JCAP* **10** (2022) 096 [2207.03102].
- [65] A. Torre and L. Quettier, *Editorial of the MADMAX Special Section*, *IEEE TAS* **33** (2023) 1.
- [66] MADMAX Collaboration, *First search for axion dark matter with a MADMAX prototype: Datasets* (2025) <https://zenodo.org/records/15496833>.
- [67] H. A. Haus, W. R. Atkinson, G. M. Branch, W. B. Davenport, W. H. Fonger, W. A. Harris et al., *Representation of noise in linear twoports*, *Proceedings of the IRE* **48** (1960) 69.

## Supplemental Material for the Letter

### First search for axion dark matter with a MADMAX prototype

#### COUPLING OF AXION FIELD TO TE<sub>11</sub> MODE: OVERLAP FORMALISM

We implemented the dielectric haloscope principle in a closed cylindrical volume. The conducting boundaries of CB200 form a waveguide in which wave propagation is described by cylindrical solutions (modes) of the wave equation. To optimize the power coupling of the axion-induced field, we maximize the transverse overlap,  $|\eta_A|$ , between the uniform axion-induced field and the mode of propagation. The TE<sub>11</sub>-mode maximizes power coupling and  $|\eta_A|$  can be calculated as:

$$|\eta_A|^2 = \frac{|\int_A dA \mathbf{E}_{\text{TE}_{11}} \cdot \hat{y}|^2}{A \int_A dA |\mathbf{E}_{\text{TE}_{11}}|^2} = 0.84, \quad (\text{S1})$$

with  $A$  the transverse area of the booster and  $\mathbf{E}_{\text{TE}_{11}}$  the electric field distribution of the TE<sub>11</sub> mode. This value can be interpreted as a scaling form-factor that reduces  $\beta^2$ . It is independent of frequency and applies for any ideal configuration of the booster implemented in cylindrical boundary conditions under the TE<sub>11</sub> mode. It is therefore implicitly included everywhere in our  $\beta^2$  calculations.

The TE<sub>11</sub> cylindrical wave propagates along the main axis where the transverse field distribution is mainly unchanged due to symmetry. To simplify the analysis, it is common to decouple the propagation direction, treating the problem as 1D. This approach is advantageous because it requires relatively few well-defined parameters to determine  $\beta^2$ . Such a single mode booster model was already demonstrated to fit the complex reflection coefficient S11 obtained from the response of the booster [42].

#### SIMULATION OF THE ELECTROMAGNETIC (EM) BOOSTER RESPONSE

A large booster diameter, much larger than the wavelength, is required to increase sensitivity. This results in a high number of parasitic modes. Mode-crossings between the desired and parasitic modes alter the field distribution and degrade the axion signal. While the single mode booster model can be used for properly describing the booster mode, finite element simulations are needed to understand the complex over-moded behavior that includes the parasitic modes. Such simulations, including the taper, the Rexolite<sup>TM</sup> lens and the booster geometries implemented in COMSOL<sup>TM</sup> using the corresponding material constants, were performed.

Different booster configurations are modeled by adapting the spacing between the disks and the mirror and the distance to the taper aperture,  $L$ . Losses are accounted for by the loss tangent of the dielectric lens and disks and the finite conductivity of all metallic walls. The attenuation of the lens is estimated to be  $< 0.1$  dB. The simulations show that with increasing  $L$  modes originating from the taper are shifted in frequency. In contrast to this, the booster mode is unchanged compared to the rest of the spectrum. Modifying  $L$  can therefore be used to avoid crossings with parasitic modes.

The key outcomes of the simulations are:

1. We have established a procedure to tune the frequency of the booster mode and avoid mode crossings.
2. We have verified that with sufficient frequency separation between the parasitic resonances and the desired booster mode, the field distribution and booster line remain largely unaffected, allowing the booster mode to be well fitted by the single mode booster model.
3. We can identify parasitic modes in regions of the spectrum near the booster mode.

The outlined strategy has been used throughout the experiment to tune the frequency of the booster mode at multiple frequencies in the 18 to 21 GHz range.

Misalignment can introduce asymmetry in the E-field, thereby affecting the E-field of the booster mode. In the current resonant configuration the strongest effect arises from the strong field between reflective mirror and first disk, which makes the mode sensitive to a mirror tilt. Our measurements also show sensitivity to mirror tilt during the tuning process. COMSOL<sup>TM</sup> simulations have shown that the typical tilts seen in our setup have only a perturbative effect on the field distribution of the booster mode. This leads to relatively small boost factor degradation, even for relatively large tilts of up to  $0.2^\circ$  corresponding to a  $\approx 350 \mu\text{m}$  offset at the mirror edge, which shift the booster mode

frequency by around 15 MHz and decrease the boost factor by up to 15%. These effects are well within the range accounted for by the single mode booster model used to fit the physics run power spectra and are included in the uncertainty budget on boost factor determination [Table I](#).

### VERIFICATION OF THE BOOSTER MODE

Direct E-field measurements using the bead-pull method [45] were used to confirm that the E-field of the booster mode follows the expected shape of a  $TE_{11}$  mode. The setup used is reported in figure [Fig. S1](#) (left). The measurement is conducted along a single axis, perpendicular to the polarization, resulting in a radial 1D field profile along the entire diameter of the booster. In figure [Fig. S1](#) (right) we report the measured electric field as a function of frequency. The field profile of the booster mode shows a well-defined single peak as expected for the case of a  $TE_{11}$  mode. Parasitic modes are easily identifiable by their higher-order variations in the field profile. Consistent behavior of the field distribution has been reproduced throughout the preparation of all booster configurations.

### FURTHER INFORMATION ON DATA TAKING

The experimental setup during data taking is shown in [Fig. S2](#). The B-field data referred to in the main text and shown in [Fig. S3](#) were taken using a Lakeshore model 475 DSP gaussmeter. The B-field probe was attached to the top of the CB200 cylinder,  $\approx 11$  cm above the center of the magnet bore. CB200 was placed within the magnet with the mirror centered within the length of the magnet bore to 1 cm precision. 3D measurements of the magnetic field performed by the CERN magnet group demonstrated that the uncertainty on the B-field strength is 2%, which has negligible impact on the  $|g_{a\gamma}|$  limit.

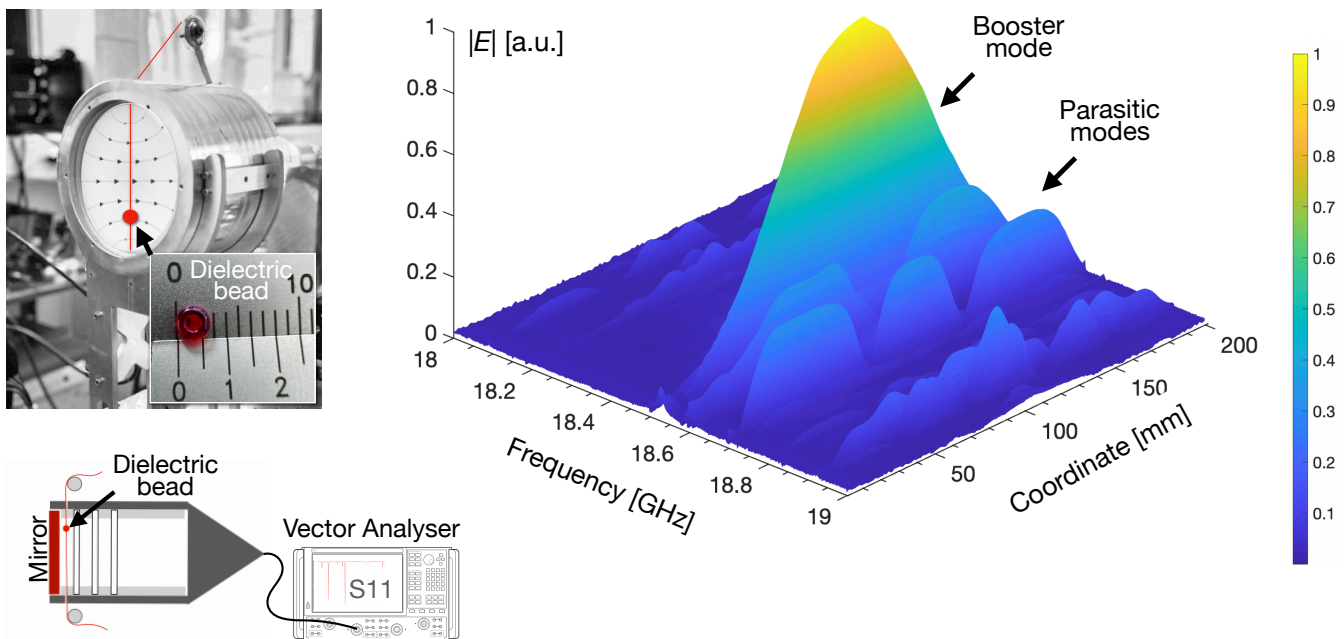


Figure S1: Details of the bead-pull measurement used to identify the booster mode. Left: Schematic of the bead-pull implementation and a photo of the opened setup. The expected E-field of the desired  $TE_{11}$  mode and a sketch of the bead are overlaid on the photo. The E-field strength is resolved along the profile indicated by the red line near the mirror surface. Right: The measured electric field distribution is shown as a function of frequency along the diameter of the booster cavity, with the center located at the coordinate 100 mm. The field profile of the booster mode exhibits a well-defined single peak, consistent with the expected the  $TE_{11}$  mode.

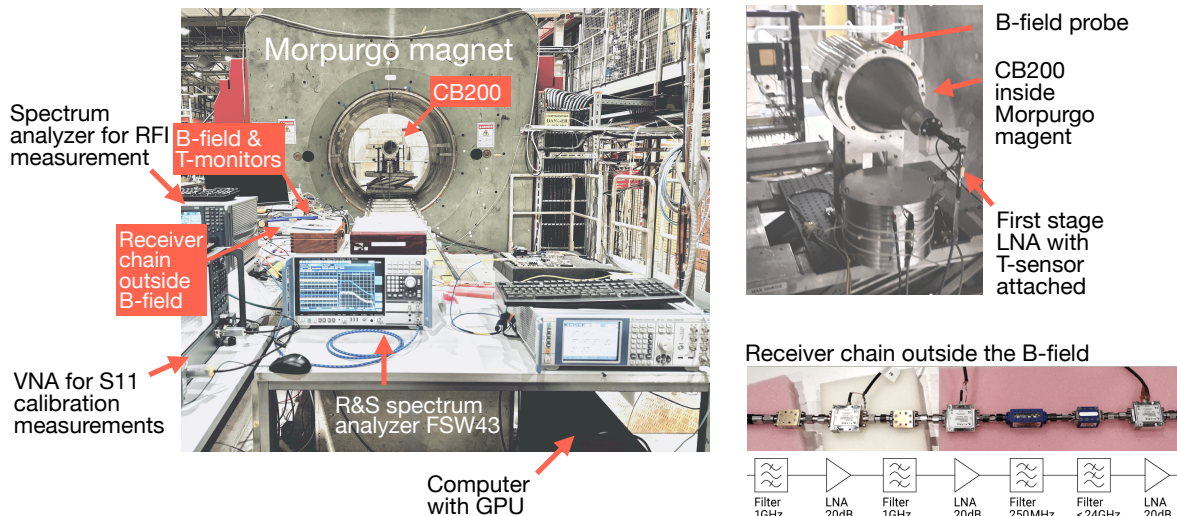


Figure S2: Left and top right: Picture of CB200 inside the Morpurgo magnet and equipment for data taking and data monitoring. Bottom right: Receiver chain components outside the B-field.

Table S1 summarizes the data taken during the individual runs, specifying the boost factor peak maximum, the frequency range in which data has been taken, the median B-field during the run, the number of individual 14.75 minute files and the corresponding integration time of the overall run. The measured B-field as a function of time is shown in Fig. S3. The median change of the B-field in between individual 14.75 minute files was 0.15 mT leading to negligible uncertainty on the limit.

### Y-FACTOR CALIBRATION

In order to calibrate the gain of the receiver chain a Y-factor calibration was performed using a noise source Keysight 346C directly connected to an attenuator of  $50\ \Omega$  impedance with attenuation  $A=30\ \text{dB}$ . At room temperature and for our frequency range of interest we work with the Rayleigh-Jeans approximation of Planck's law for the noise power  $P_N$ :

$$P_N = k_B B T \quad (\text{S2})$$

with  $k_B$  the Boltzmann constant,  $B$  the resolution bandwidth of the receiver and  $T$  the equivalent noise temperature. The warm and cold measurements of the Y-factor calibration correspond to the noise source being switched on and off. For both cases, the expected noise power has two contributions: one is coming from the equivalent noise temperature of the amplifier the other from the attenuator with noise source attached. With the noise source off, the attenuator

Table S1: Overview over datasets taken.

$\beta^2$ Peak maximum	Frequency region	Median B-field	Number of 14.75 min. files	Corresponding integration time
[GHz]	[GHz]	[T]		[h]
18.531	18.513-18.575	1.58	54	13.28
18.543	18.513-18.575	1.01	295	72.53
18.557	18.513-18.575	1.01	636	156.38
19.196	19.177-19.230	1.27	163	40.08
19.215	19.177-19.230	1.58	245	60.24



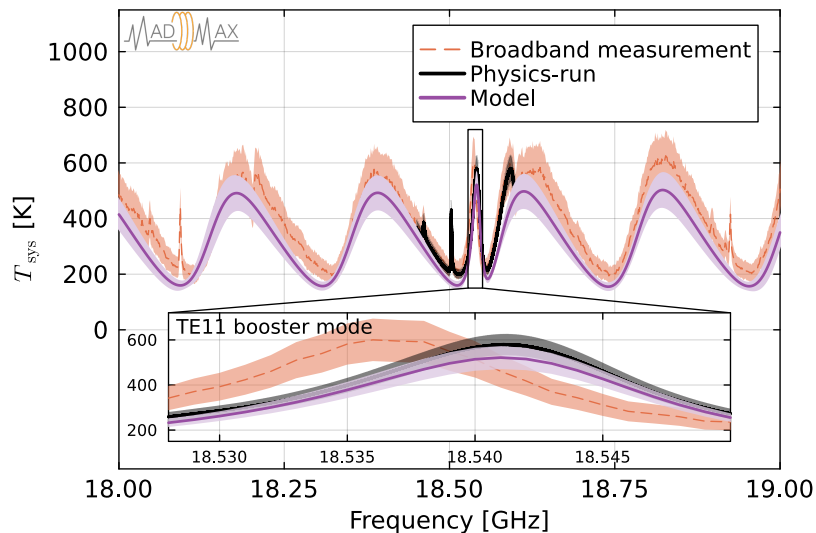


Figure S4: Exemplary system temperature spectra ( $T_{\text{sys}}$ ) obtained from broadband measurements (dashed red) and from an axion physics-run (solid black). For the latter, only a reduced frequency range around the  $\text{TE}_{11}$  mode resonance is recorded. The  $T_{\text{sys}}$  spectrum obtained from the booster model (solid magenta) is superimposed with the band around the line indicating the systematic uncertainties. For the physics-run power spectrum, a zoom to the  $\text{TE}_{11}$  booster mode region is shown in the inset and a good agreement with the model is observed.

parameters. The value for  $d$  is extracted from a fit to the calibration broadband measurement. The change in boost factor due to the connected amplifier is quantified by the factor

$$F_{RC} = \frac{1 - |\Gamma_{\text{LNA}}|^2}{|1 - e^{-2i\omega d} \Gamma_b \Gamma_{\text{LNA}}|^2} \quad (\text{S4})$$

with the boosters and LNA reflectivities  $\Gamma_b$  and  $\Gamma_{\text{LNA}}$ .

The booster noise has a significant contribution of  $\approx 150$ - $200$  K at the boosters  $\text{TE}_{11}$  resonance frequency. It results from the following components:

1. waveguide, taper and lens. These are modeled by one single attenuation contributing with roughly 10 K noise

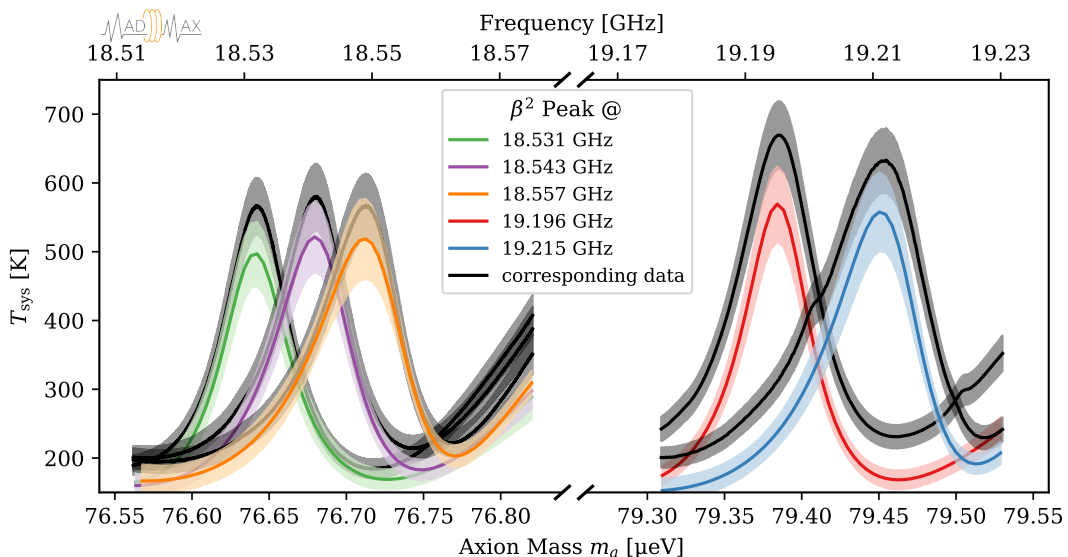


Figure S5: Simulation and data for each physics-run's power spectrum around the  $\text{TE}_{11}$  booster mode.

Table S2: Summary of frequency bands relevant in the data taking, calibration and analysis procedure.

	Frequency	Description
Raw data bins resolution bandwidth	9 Hz	Given by inverse of coherent integration time of DAQ, i.e. the length of the individual time domain signal traces with 110 ms length which are FFT-ed.
Analysis data bins resolution bandwidth	0.9 kHz	Chosen such that frequency resolution is good enough to resolve a potential axion signal-width.
FWHM of Axion, signal width	20 kHz	Given by DM velocity dispersion of galactic DM halo
Boost factor band width	10 MHz	Depends on booster configuration. In this case with 3 disks we are using resonant configuration determined by distance between mirror and first disk corresponding to roughly $\lambda/2$ of resonant frequency.
Receiver bandwidth physics runs	250 MHz	Adapted to boost factor width and scan width. Determined by pass band filters in front of receiver system and by its settings.
Spectrum analyzer bandwidth during calibration	1 GHz	Determined by peak to peak fluctuation length (in frequency domain) of Fabry-Perot oscillation pattern due to LNA noise induced standing wave between LNA and booster.

temperature,

- the disks, that, from the effective loss determined in the fitting procedure, have a noise temperature of  $\approx 0.03$  K each and
- the mirror with a noise temperature of  $\approx 0.3$  K, determined by its absorption calculated from its conductivity.

Outside the boosters  $TE_{11}$  resonance, the simulated booster noise oscillates around  $\approx 10$  K, matching the incoherent sum of those components. On resonance, as a very rough estimate, the  $\approx 0.3$  K equivalent noise temperature of the mirror can be multiplied by the boost factor of  $\mathcal{O}(10^3)$  to get to the maximum noise contribution of  $\mathcal{O}(10^2)$  K of the booster.

Simulated and measured system noise temperature for all five physics runs are shown in Fig. S5. The model reproduces the frequency position of the resonance peaks. System temperature is consistently slightly underestimated, which does not affect the boost factor determination, as only the frequency dependence of  $T_{\text{sys}}$  is used in the analysis.

## FURTHER INFORMATION

Data taking and analysis involve many different frequency bands. They are summarized and commented in Table S2. Fig. S6 Shows the power excess in each individual frequency bin after cross correlation with the expected axion signal shape.

Fig. S7 shows a zoom of the limit plot at the axion mass range with highest sensitivity. The bin to bin fluctuation of the limits and the truncation below the 16% quantile are clearly visible, as are correlations between adjacent frequency bins. The latter arise due to cross-correlation with the axion line-shape as mentioned in the text.

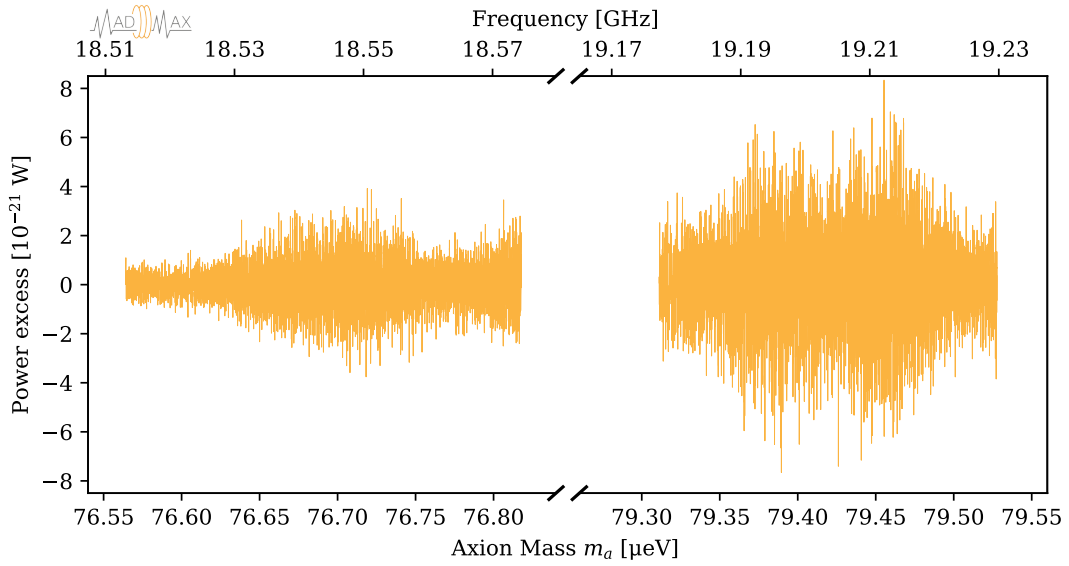


Figure S6: Observed cross-correlated power excess as a function of frequency.

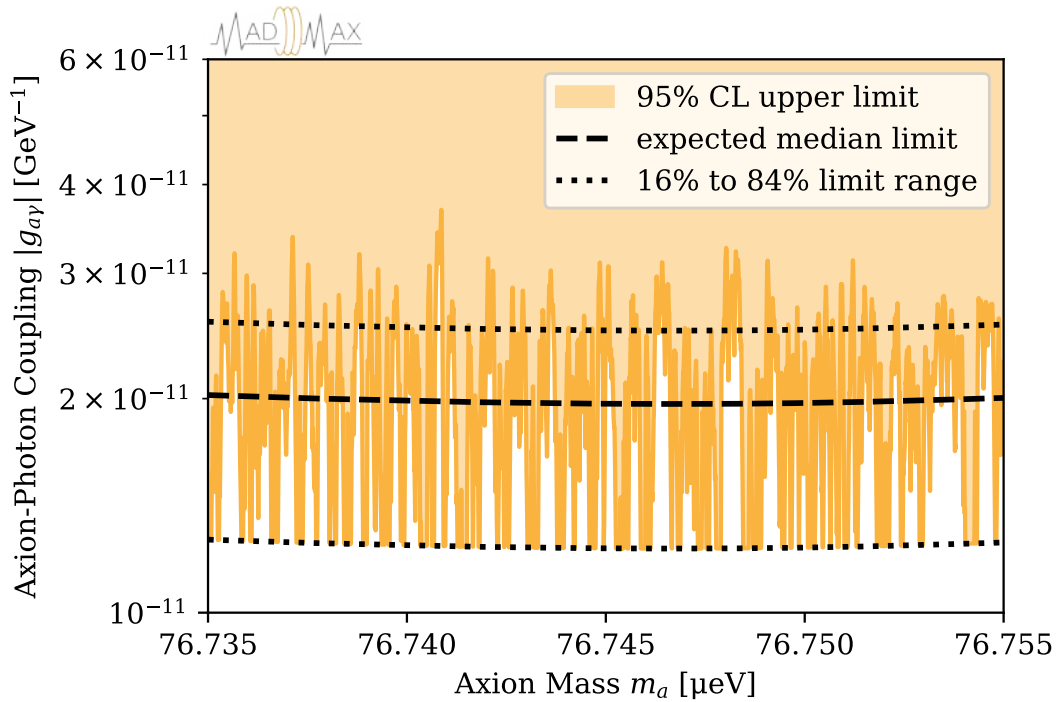


Figure S7: 95% CL exclusion limit around the most sensitive region for configuration 1.